Investigation of mixing and diffusion processes in hybrid spot laser–MIG keyhole welding

2009 J. Phys. D: Appl. Phys. 42 095502

(http://iopscience.iop.org/0022-3727/42/9/095502)

IOP PUBLISHING JOURNAL OF PHYSICS D: APPLIED PHYSICS

J. Phys. D: Appl. Phys. **42** (2009) 095502 (15pp) doi:10.1088/0022-3727/42/9/095502

Investigation of mixing and diffusion processes in hybrid spot laser–MIG keyhole welding

J Zhou[1] **and H L Tsai**[2]

[1] Mechanical Engineering, The Pennsylvania State University Erie, The Behrend College, 1501 Jordan Road, Erie, PA 16563, USA
[2] Department of Mechanical and Aerospace Engineering, Missouri University of Science and Technology, 400 W. 13th St., Rolla, MO 65409-0500, USA

E-mail: juz17@psu.edu

Received 20 November 2008, in final form 3 March 2009
Published 17 April 2009
Online at stacks.iop.org/JPhysD/42/095502

Abstract
In hybrid laser–MIG keyhole welding, anti-crack elements can be added into the weld pool through a filler metal in anticipation of compensating mass loss, preventing porosity formation and improving compositional and mechanical properties of the welds. Understanding the mixing and diffusion of the filler metal in the molten pool is vital to achieve these desired objectives. In this study, mathematical models and associated numerical techniques have been developed to investigate the mixing and diffusion processes in hybrid laser–MIG keyhole welding. The transient interactions between droplets and weld pool and dynamics of the melt flow are studied. The effects of key process parameters, such as droplet size (wire diameter), droplet generation frequency (wire feed speed) and droplet impinging speed, on mixing/diffusion are systematically investigated. It was found that compositional homogeneity of the weld pool is determined by the competition between the mixing rate and the solidification rate. A small-size filler droplet together with high generation frequency can increase the latitudinal diffusion of the filler metal into the weld pool, while the large-size droplet along with the low generation frequency helps to get more uniform longitudinal diffusion. Increasing the impinging velocity of the filler droplet can improve the latitudinal diffusion of the filler metal. However, a high impinging velocity can cause a lower diffusion zone in the upper part of the welds. This study provides a good foundation for optimizing the hybrid laser–MIG keyhole welding process to achieve quality welds with desired properties.

1. Introduction

Laser keyhole welding is characterized by high precision, deep penetration depths, low heat input and weldment distortion, and high welding speed [1, 2]. However, when a laser is used to weld certain alloys, such as 5000 and 6000 series aluminium alloys which are desired by the auto industry for their excellent corrosion resistance and substantial strength [3], the low melting-point elements, such as aluminium or magnesium, are easily vaporized and lost from the weld region, leading to the formation of porosity, cracking susceptibility, changes of composition and mechanical properties and other defects [4–6].

As shown in some studies [7], mechanical properties, hot crack susceptibility and corrosion resistance of welds are greatly affected by the cooling rate, metal compositional and microstructural changes across the welds in the welding process. Hatch [4] found that the yield strength of 5000 series aluminium alloys increased linearly with the concentration of magnesium. He also pointed out that the corrosion resistance of the alloys was deteriorated by the metal composition change. Cieslak and Fuerschbach [5] reported that the vaporization of magnesium in laser welding resulted in reduced metal hardness. Dudas and Collins [6] concluded that the hot crack susceptibility of aluminium alloys was dependent on their compositions. Since in laser welding the cooling rate is very high, serious hot cracks are frequently observed in laser welding of aluminium alloys.

Hybrid laser–MIG welding, by combining laser welding and arc welding together, can eliminate undercuts, change microstructures and alter mechanical properties of the welds [8–12]. In hybrid laser welding, by adding anti-crack elements through the filler metal, the aforementioned problems, such as hot crack susceptibility and strength reduction can be mitigated or eliminated. Missouri and Sili [13] reported that adding filler metal could offer advantages in the chemical composition of the weld zone, which could have a positive effect on the impact toughness and on the resistance to porosity for laser welding of high-strength structural steels. Hwang *et al* [14] suggested that the added filler wire material had positive effects on fatigue properties of SPCC-CQ1 cold rolled steel. Schubert *et al* [15] proposed that the formation of hot cracks in aluminium welding was determined by the temperature–time-cycle, mixing and chemical compositions in regions of high crack sensitivities. Moore *et al* [16] found that microstructure and toughness of the hybrid welds of carbon–manganese steels were improved significantly by the addition of filler metals in the hybrid process. Hu and Richardson [17] concluded that the added filler metal could improve ductility and increase strength of the hybrid AA7075 (T6) welds. Apparently, in order to achieve these desired objectives, it is a prerequisite that the filler metal can mix and diffuse well into the weld pool. Hence, it is important to study the mixing and diffusion of filler metal in the weld pool to determine the key process parameters dominating the mixing and diffusion processes.

Research on hybrid laser welding is focused mainly on effectively combining a laser welding process together with an arc welding process [8–12] and on investigations of the effects of process parameters, such as arc and shielding gas, on welds quality [17–21] using experimental methods. In recent years, some research has been conducted to study the transport phenomena, such as the heat transfer process, in hybrid laser welding [22, 23]. Some preliminary studies have been done by Zhao and Debroy [24] to study the compositional changes in conduction mode laser welding. However, very limited research exists focusing on the study of the complicated droplet–weld pool interaction and the processes of mixing and diffusion in hybrid laser welding. Obviously, understanding these phenomena is vital to optimize the hybrid laser–MIG welding process to obtain quality hybrid welds. In this paper, hybrid laser–MIG keyhole welding models developed by Zhou [22] are modified and extended to study the mixing and diffusion processes in hybrid laser–MIG welding. The models include the calculation of temperature field, pressure balance, melt flow, free surface, laser-induced plasma and multiple reflections. The transient energy transport in the weld pool and the keyhole plasma are both investigated. However, the main focus of this study is on the investigation of the mixing and diffusion of filler droplets in the weld pool, weld pool dynamics and the effects of adding filler droplets on the compositional changes in the welds.

2. Mathematical model

Figure 1 shows a schematic sketch of a pulsed laser keyhole welding process. A control volume method employing the volume of fluid (VOF) technique [25] and the continuum formulation [26] is used to calculate the momentum and energy transport in the weld pool. The VOF technique can handle a transient deformed weld pool surface, while the continuum formulation can handle fusion and solidification for the liquid region, the mush zone and the solid region. Plasma in the keyhole is treated as the vapour of weld material. Although the velocity and pressure change dramatically across the Knudsen layer, the generic translation vapour flow along the keyhole is neglected [27] and, in this study, only the temperature distribution is considered. Meanwhile, the pressure along the keyhole is also considered to be approximately constant [28] and is comparable to the atmospheric pressure. Note in high power laser welding ($\geqslant$8 kW), the plasma plume and its velocities in the keyhole can be very significant [29], hence, the assumption of no plasma flow in this study is limited to low power laser keyhole welding.

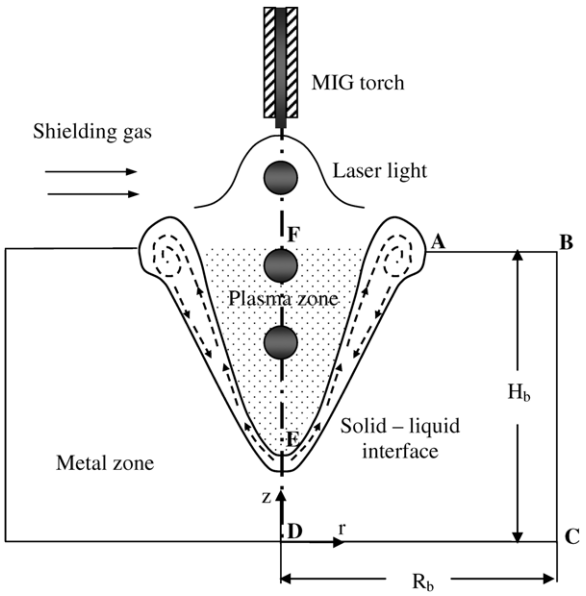

Figure 1. Schematic sketch of spot hybrid laser–MIG keyhole welding.

2.1. Metal zone simulation

2.1.1. Governing equations. The governing differential equations used to describe the heat and mass transfer and fluid flow in a cylindrical coordinate (r–z) system given by Chiang and Tsai [26] are modified and used in this study:

Continuity

$$\frac{\partial}{\partial t}(\rho) + \nabla \cdot (\rho \boldsymbol{V}) = 0. \tag{1}$$

Momentum

$$\frac{\partial}{\partial t}(\rho u) + \nabla \cdot (\rho \boldsymbol{V} u) = \nabla \cdot \left(\mu_1 \frac{\rho}{\rho_1} \nabla u\right) - \frac{\partial p}{\partial r} - \frac{u_1}{K}\frac{\rho}{\rho_1}(u - u_s) - \frac{C\rho^2}{K^{0.5}\rho_1}|u - u_s|(u - u_s) - \nabla \cdot (\rho f_s f_l \boldsymbol{V}_r u_r) + \nabla \cdot \left(\mu_s u \nabla \left(\frac{\rho}{\rho_1}\right)\right), \tag{2}$$

$$\frac{\partial}{\partial t}(\rho v) + \nabla \cdot (\rho \boldsymbol{V} v) = \rho g + \nabla \cdot \left(\mu_l \frac{\rho}{\rho_l} \nabla v\right) - \frac{\partial p}{\partial z} - \frac{u_l}{K}\frac{\rho}{\rho_l}(v - v_s) - \frac{C\rho^2}{K^{0.5}\rho_l}|v - v_s|(v - v_s) - \nabla \cdot (\rho f_s f_l \boldsymbol{V}_r v_r) + \nabla \cdot \left(\mu_s v \nabla \left(\frac{\rho}{\rho_l}\right)\right) + \rho g \beta_T (T - T_0). \quad (3)$$

Energy

$$\frac{\partial}{\partial t}(\rho h) + \nabla \cdot (\rho \boldsymbol{V} h) = \nabla \cdot \left(\frac{k}{c_p} \nabla h\right) - \nabla \cdot \left(\frac{k}{c_p} \nabla (h_s - h)\right) - \nabla \cdot (\rho(\boldsymbol{V} - \boldsymbol{V}_s)(h_l - h)). \quad (4)$$

Species

$$\frac{\partial}{\partial t}(\rho f^\alpha) + \nabla \cdot (\rho \boldsymbol{V} f^\alpha) = \nabla \cdot (\rho D \nabla f^\alpha) - \nabla \cdot \left(\rho D \nabla (f_l^\alpha - f^\alpha)\right) - \nabla \cdot \left(\rho(\boldsymbol{V} - \boldsymbol{V}_s)(f_l^\alpha - f^\alpha)\right). \quad (5)$$

The physical meaning of each term appearing in the above equations can be found in [26]. In equations (1)–(5), the continuum density, specific heat, thermal conductivity, solid mass fraction, liquid mass fraction, mass diffusivity, velocity and enthalpy are defined in [30].

2.2. Tracking of free surfaces

The algorithm of VOF is used to track the dynamics of free surfaces. The fluid configuration is defined by a VOF function, $F(r, z, t)$, which tracks the location of the free surface. The function F takes the value of one for the cell full of fluid and the value of zero for the empty cell. Cells with F values between zero and one are partially filled with fluid and identified as surface cells. The function F is governed by the following equation:

$$\frac{\mathrm{d}F}{\mathrm{d}t} = \frac{\partial F}{\partial t} + (\boldsymbol{V} \cdot \nabla) F = 0. \quad (6)$$

2.3. Boundary conditions

The boundaries of the metal zone simulation are divided into five segments, as shown in figure 1.

2.3.1. Top surface inside the keyhole (AE in figure 1). For cells containing the free surface, that is, cells that contain fluid but have one or more empty neighbours, in the direction normal to the free surface, the following pressure condition must be satisfied [1]:

$$P = P_\sigma + P_r, \quad (7)$$

where P is the pressure at the free surface in a direction normal to the local free surface. P_σ is the surface tension and P_r is the recoil pressure. P_σ is calculated by the following formula:

$$P_\sigma = \kappa \gamma, \quad (8)$$

where κ is the free surface curvature, given by [29]:

$$\kappa = -\left[\nabla \cdot \left(\frac{\vec{n}}{|\vec{n}|}\right)\right] = \frac{1}{|\vec{n}|}\left[\left(\frac{\vec{n}}{|\vec{n}|} \cdot \nabla\right)|\vec{n}| - (\nabla \cdot \vec{n})\right], \quad (9)$$

where $\vec{n}$ is the unit vector normal to the local free surface. For a pseudo-binary Fe–S system, the surface tension coefficient γ can be calculated as a function of temperature T and sulfur concentration f^α [31]:

$$\gamma = 1.943 - 4.3 \times 10^{-4}(T - 1723) - RT \times 1.3 \times 10^{-8} \ln\left[1 + 0.00318 f^\alpha \exp\left(\frac{1.66 \times 10^8}{RT}\right)\right]. \quad (10)$$

In this study, the temperature and concentration dependent Marangoni shear stress on the free surface in the direction tangential to the local surface is given by [32]:

$$\tau_{\vec{s}} = \mu_l \frac{\partial (V \cdot \vec{s})}{\partial \vec{n}} = \frac{\partial \gamma}{\partial T}\frac{\partial T}{\partial \vec{s}} + \frac{\partial \gamma}{\partial f^\alpha}\frac{\partial f^\alpha}{\partial \vec{s}}. \quad (11)$$

Calculation of the evaporation-induced recoil pressure P_r is complicated by the existence of a Knudsen layer over the vaporizing surface. Based on Knight's model [33], the recoil pressure can be calculated by [34]

$$P_r = A B_0 / \sqrt{T_w} \exp(-U/T_w), \quad (12)$$

where A is the numerical coefficient and B_0 is the vaporization constant. The coefficient A depends on the ambient pressure and its value varies from 0.55 for evaporation in the vacuum to 1 for the case of evaporation under a high ambient pressure. For atmospheric pressure, the coefficient A is close to its minimal value of 0.55. B_0 is at the value of 1.78×10^{10}. T_w is the surface temperature of the liquid metal on the keyhole wall. The parameter U is defined as follows [35]:

$$U = m_a H_v / (N_a k_b), \quad (13)$$

where m_a is atomic mass, H_v is the latent heat of evaporation, N_a is Avogadro's number and k_b is Boltzmann's constant.

The energy on the top free surface is balanced between the laser irradiation, plasma-keyhole wall radiation, the heat dissipation through convection, and metal vaporization. In general, since the velocity of the plume along the surface is assumed to be zero [10], the heat loss due to convection is omitted. The energy balance is given by the following formula:

$$k \frac{\partial T}{\partial \vec{n}} = q_{laser} + q_{rad} - q_{evap}. \quad (14)$$

In this study, the liquid/vapour evaporation model is used due to the low intensity of laser irradiation. The heat loss due to surface evaporation can be written as [35]

$$q_{evap} = W H_v, \quad (15)$$

$$\log(W) = A_v + \left(6.121 - \frac{18836}{T}\right) - 0.5 \log T. \quad (16)$$

The laser heat flux q_{laser} comes from the Fresnel absorption of the incident intensity directly from the laser beam plus the incident intensity from the multiple reflections:

$$q_{\text{laser}} = I_{\text{o}}(r, z)\alpha_{\text{Fr}}(\varphi_{\text{o}}) + \sum_{m=1}^{n} I_{\text{r},m}(r, z)\alpha_{\text{Fr}}(\varphi_m), \tag{17}$$

$$\alpha_{\text{Fr}}(\varphi) = 1 - \frac{1}{2}\left(\frac{1 + (1 - \varepsilon_{\text{f}}\cos\varphi)^2}{1 + (1 + \varepsilon_{\text{f}}\cos\varphi)^2} + \frac{\varepsilon_{\text{f}}^2 - 2\varepsilon_{\text{f}}\cos\varphi + 2\cos^2\varphi}{\varepsilon_{\text{f}}^2 + 2\varepsilon_{\text{f}}\cos\varphi + 2\cos^2\varphi}\right), \tag{18}$$

where φ is the angle of the incident light with the normal of the keyhole surface, n is the total number of incident lights from multiple reflections. ε_{f} is a material-dependent coefficient. In CO_2 laser welding of mild steel, $\varepsilon_{\text{f}} = 0.2$ is used. $I_{\text{o}}(r, z)$ and $I_{\text{r},m}(r, z)$ are, respectively, the incident intensity from laser beam and the mth multiple reflection at the keyhole wall which are given as

$$I_{\text{o}}(r, z) = I_{\text{c}}(r)\exp\left(-\int_0^{z_0} K_{\text{pl}}\,\text{d}z\right), \tag{19}$$

$$I_{\text{r},m}(r, z) = I_{\text{r}}(r, z)\exp\left(-\int_0^{z_m} K_{\text{pl}}\,\text{d}z\right), \tag{20}$$

$$I_{\text{r}}(r, z) = I_{\text{o}}(r, z)(1 - \alpha_{\text{Fr}}), \tag{21}$$

where $I_{\text{c}}(r)$ stands for the original collimated incident laser beam intensity, $I_{\text{r},m}(r, z)$ is the reflected laser beam intensity at the m times reflections, $\int_0^{z_0} K_{\text{pl}}\,\text{d}z$ and $\int_0^{z_m} K_{\text{pl}}\,\text{d}z$ are the optical thicknesses of the laser transportation path, respectively, for the first incident and the multiple reflections and K_{pl} is the plasma absorption coefficient due to the inverse bremsstrahlung (IB) absorption [36]

$$K_{\text{pl}} = \frac{n_{\text{e}}n_{\text{i}}Z^2e^6 2\pi}{6\sqrt{3}m\varepsilon_0^3 c\bar{h}\omega^3 m_{\text{e}}^2}\left(\frac{m_{\text{e}}}{2\pi k_{\text{b}}T_{\text{pl}}}\right)^{0.5} \times\left[1 - \exp\left(-\frac{\omega}{k_{\text{b}}T_{\text{pl}}}\right)\right]\bar{g}, \tag{22}$$

where Z is the charge of ion in the plasma, e is the charge of electrons, ω is the angular frequency of the laser irradiation, ε_0 is the dielectric constant, n_{e} and n_{i} are the densities of electrons and ions respectively, $\bar{h}$ is Planck's constant, m is a constant that is related to the specific laser being used and is assigned one for CO_2 laser, m_{e} is the electron mass, T_{pl} is the plasma temperature, c is the speed of light, and $\bar{g}$ is the quantum mechanical Gaunt factor. For weakly ionized plasma in the keyhole, Saha equation [37] can be used to calculate the densities of the plasma species:

$$\frac{n_{\text{e}}n_{\text{i}}}{n_0} = \frac{g_{\text{e}}g_{\text{i}}}{g_0}\frac{(2\pi m_{\text{e}}k_{\text{b}}T_{\text{pl}})^{1.5}}{\bar{h}^3}\exp\left(-\frac{E_{\text{i}}}{k_{\text{b}}T_{\text{pl}}}\right), \tag{23}$$

where n_0 is neutral particle density which is 10^{26} cm^{-3} for iron [38], g_{e}, g_{i} and g_0 are, respectively, the degeneracy factors for electrons, ions and neutral atoms, E_{i} is the ionization potential for the neutral atoms in the gas. Assuming the laser intensity distribution is ideal Gaussian-like, $I_{\text{c}}(r)$ can be written as [38]

$$I_{\text{c}}(r) = \frac{2P_{\text{laser}}}{\pi r_{\text{fo}}^2}\left(\frac{r_{\text{f}}}{r_{\text{fo}}}\right)^2\exp\left(-\frac{2r^2}{r_{\text{f}}^2}\right), \tag{24}$$

where r_{f} is the beam radius, r_{fo} is the beam radius at the focal position and P_{laser} is the laser power. In laser welding, the keyhole surface temperature is much lower than that of the plasma, so the radiation and emission of the surface can be omitted. Then q_{rad} can be simplified as

$$q_{\text{rad}} = \varepsilon\sigma(\overline{T_{\text{pl}}}^4 - T^4), \tag{25}$$

where $\overline{T_{\text{pl}}}$ is the average temperature of keyhole plasma.

2.3.2. Top surface outside the keyhole (AB in figure 1). Boundary condition on the top surface outside the keyhole is similar to that inside the keyhole. The differences lie in the absence of plasma and multiple reflections. As shown in figure 1, there is a shielding gas flow above the base metal, which means that plasma outside the keyhole will be blown away. So equation (17) can be written as

$$q_{\text{laser}} = I_{\text{o}}(r, z)\alpha_{\text{Fr}}\cos\varphi. \tag{26}$$

Since there is no plasma and the temperature of shielding gas is much lower than that of the metal surface, the radiation heat flux can be given as

$$q_{\text{rad}} = -\varepsilon\sigma(T^4 - T_\infty^4). \tag{27}$$

Here, T_∞ is the ambient temperature. Since there is a shielding gas flow over the surface, the convection heat loss cannot be omitted which is given by

$$q_{\text{conv}} = h_{\text{conv}}(T - T_\infty). \tag{28}$$

The boundary condition for the species equation on the top surface is given by

$$\frac{\partial f^\alpha}{\partial z} = 0. \tag{29}$$

2.3.3. Side surface (BC in figure 1).

$$-k\frac{\partial T}{\partial r} = q_{\text{conv}}, \tag{30}$$

$$u = 0, v = 0, \tag{31}$$

$$\frac{\partial f^\alpha}{\partial r} = 0. \tag{32}$$

2.3.4. Bottom surface (CD in figure 1).

$$-k\frac{\partial T}{\partial z} = q_{\text{conv}}, \tag{33}$$

$$u = 0, v = 0, \tag{34}$$

$$\frac{\partial f^\alpha}{\partial z} = 0. \tag{35}$$

2.3.5. Symmetrical axis (DE in figure 1).

$$\frac{\partial T}{\partial r} = 0, \tag{36}$$

$$u = 0, \frac{\partial v}{\partial r} = 0, \tag{37}$$

$$\frac{\partial f^{\alpha}}{\partial r} = 0. \tag{38}$$

2.4. Plasma zone simulation

2.4.1. Governing equations. In this study, metal vapour in the keyhole is assumed to be a compressible, inviscid ideal gas. Since the heat production by viscous dissipation is rather small in laser welding, the energy equation can be simplified as [39]

$$\frac{\partial}{\partial t}(\rho_{\rm pl} h_{\rm pl}) = \nabla \cdot \left(\frac{k_{\rm pl}}{c_{\rm pl}} \nabla h_{\rm pl} - \boldsymbol{q}_{\rm r}\right) + K_{\rm pl} I_{\rm c}(r) \exp\left(-\int_0^{z_o} K_{\rm pl}\, {\rm d}z\right) + \sum_{m=1}^{n} K_{\rm pl} I_{{\rm r},m}(r, z) \exp\left(-\int_0^{z_m} K_{\rm pl}\, {\rm d}z\right), \tag{39}$$

where $h_{\rm pl}$ and $\rho_{\rm pl}$ represent, respectively, the enthalpy and density of the plasma, $k_{\rm pl}$ and $c_{\rm pl}$ represent, respectively, the thermal conductivity and specific heat of the plasma. $\boldsymbol{q}_{\rm r}$ stands for the radiation heat flux vector. Note $h_{\rm pl} = c_{\rm pl} T_{\rm pl}$.

The radiation source term $\nabla \cdot (\boldsymbol{q}_{\rm r})$ is defined as

$$\nabla \cdot \boldsymbol{q}_{\rm r} = k_{\rm a}\left(4\pi I_{\rm b} - \int_{4\pi} I\, {\rm d}\Omega\right), \tag{40}$$

where $k_{\rm a}$, $I_{\rm b}$ and Ω denote the Planck mean absorption coefficient, blackbody emission intensity ($I_{\rm b} = \sigma T_{\rm pl}^4$) and solid angle, respectively. When an intense laser pulse interacts with the vapour in the keyhole, a significant amount of laser irradiation is absorbed by the ionized particles through the IB absorption. For simplicity, the plasma is assumed to be an absorbing–emitting medium and the scattering effect is neglected. The radiation transport equation (RTE) has to be solved for the total directional radiative intensity $I(\boldsymbol{r}, \boldsymbol{s})$ [40]:

$$(\boldsymbol{s} \cdot \nabla) I(\boldsymbol{r}, \boldsymbol{s}) = k_{\rm a}(I_{\rm b} - I(\boldsymbol{r}, \boldsymbol{s})), \tag{41}$$

where $\boldsymbol{s}$ and $\boldsymbol{r}$ denote a unit vector along the direction of the radiation intensity and the local position vector. When the plume within the keyhole is weakly ionized, the absorption mechanism depends mainly on electron–neutral interaction and the plume behaves as an optically thin medium. For the evaluation of the intensity and heat flux divergence, the Planck mean absorption coefficient is given as [40]

$$k_{\rm a} = \left(\frac{128}{27} k_{\rm b}\right)^{0.5} \left(\frac{\pi}{m_{\rm e}}\right)^{1.5} \frac{Z^2 e^6 \overline{g}}{h\sigma c^3} \frac{n_{\rm e} n_{\rm i}}{T_{\rm pl}^{3.5}}. \tag{42}$$

2.4.2. Boundary conditions.

Bottom surface inside the keyhole (EA in figure 1). Close to the liquid wall inside the keyhole, there is a so-called Knudsen layer where vaporization of material takes place. The vapour temperature across the Knudsen layer is discontinuous, which can be calculated by the following formula [33]:

$$\frac{T_{\rm K}}{T_{\rm l}} = \left[\sqrt{1 + \pi\left(\frac{\gamma_{\rm r} - 1}{\gamma_{\rm r} + 1}\frac{m_{\rm v}}{2}\right)^2} - \sqrt{\pi}\frac{\gamma_{\rm r} - 1}{\gamma_{\rm r} + 1}\frac{m_{\rm v}}{2}\right]^2, \tag{43}$$

$$m_{\rm v} = M_{\rm k}\sqrt{\frac{2}{\gamma_{\rm r}}}, \tag{44}$$

where $T_{\rm K}$ is the vapour temperature outside of the Knudsen layer, $T_{\rm l}$ is the liquid surface temperature adjacent to the Knudsen layer, $M_{\rm k}$ is Mach number at the outer surface of the Knudsen layer and $\gamma_{\rm r}$ is the specific heat ratio. The value of $m_{\rm v}$ depends on the gas dynamics of the vapour flow away from the surface. $M_{\rm k} = 1.2$ is used in this study [32]. The vapour is assumed to be iron in the form of monatomic gas with a molecular weight of 56 and $\gamma_{\rm r} = 1.67$. The gas temperature outside the Knudsen layer is used as the boundary temperature. So the boundary condition is given by [40]

$$T_{\rm pl} = T_{\rm K}, \tag{45}$$

$$I = \varepsilon I_{\rm b} + \frac{1 - \varepsilon}{\pi} \int_{\vec{n} \cdot \Omega' < 0} I\, |\vec{n} \cdot \Omega|\, {\rm d}\Omega'. \tag{46}$$

Top surface outside the keyhole (FA in figure 1).

$$T_{\rm pl} = T_{\infty}, \tag{47}$$

$$I = I_{\rm c}(r). \tag{48}$$

Symmetrical axis (EF in figure 1).

$$\frac{\partial T_{\rm pl}}{\partial r} = 0, \tag{49}$$

$$\frac{\partial I}{\partial r} = 0. \tag{50}$$

3. Numerical methods

The solutions of transport equations in the metal zone and in the plasma zone are coupled; that is, the simulations of the metal and the plasma zone provide boundary conditions for each other. However, there are large spatial and physical differences between the metal and the plasma zone. To enhance convergence rate and save calculation time, different time and space resolutions are used for the metal and the plasma zone. The governing equations (equations (1)–(5) and (39)) and all related supplemental equations and boundary conditions are solved through the following iterative scheme:

1. Equations (1)–(4) are solved iteratively for the metal zone to obtain velocity, pressure and temperature distributions using the associated boundary conditions.

2. Equation (5) is solved for the metal zone to obtain the concentration distributions using the associated boundary conditions.
3. Equation (39) is solved iteratively to obtain the plasma temperature distributions in the keyhole under the associated boundary conditions. The steps for solving equation (39) are listed below:
   (a) Solve equation (41) using the associated boundary conditions to get the total directional radiative intensity distributions.
   (b) Solve equation (40) to get radiation source term $\nabla \cdot (\boldsymbol{q}_r)$.
   (c) Solve equations (23) and (22) in the order using the most recent plasma temperature from the previous time step to get the updated plasma absorption coefficient K_{pl}.
   (d) Solve equation (39) to get the updated plasma temperature.
4. Solve VOF algorithm equation (6) to obtain the new domain for the metal (solid + liquid) and plasma (gas) zones.
5. Update boundary conditions applied for the metal (liquid) and the plasma (gas) zones.
6. Advance to the next time step and back to step 1 until the desired time is reached.

The techniques for solving equations (1)–(5) and (39) are given by Wang and Tsai [30]. Following the MAC scheme, the r- and z-velocity components are located at cell face centres on lines of constants r and z, respectively; while the pressure, VOF function, temperature and absorbed laser flux are located at cell centres. Since the temperature and pressure field change more dramatically near the keyhole, a non-uniform grid system with 202 × 252 points is used for the total computational domain of 5.0 mm × 20.0 mm, in which smaller grids are concentrated near the keyhole and larger grids for other parts. Due to the axis-symmetry of the domain, only half of the grid points were used in the calculation. Calculations were executed on the Dell Optiplex GX270 workstations with Linux-Redhat 9.0 OS and it took about 6.3 h of CPU time to simulate about 100 ms of real-time welding. The average time step is 10^{-4} s and the smallest time step is about 10^{-6} s.

4. Results and discussion

The base metal is assumed to be 304 stainless steel containing 100 ppm sulfur. The process parameters and thermophysical properties used in this study are summarized in table 1.

Major assumptions adopted in this study are summarized as follows. The laser energy is assumed to be in the Gaussian distribution and the focus plane is on the top surface of the base metal. MIG droplets are assumed to be steadily generated via a certain wire feeding method right after the shut-off of the laser. The droplet is made of 304 stainless steel and its size, initial temperature, velocity and generation frequency are given and vary in the calculation. Arc heat and arc pressure are used as constants in this study. In the future, filler wire melting, droplet generation, arc plasma generation [41] will be integrated into current models. Note, in this study, the element 'sulfur' is used just as a media to trace the mixing and diffusion processes in the weld pool. In the calculation of the mass transfer (species) equation, the 'sulfur' itself will not have any effect on it. In

Table 1. Thermophysical properties of 304 stainless steel and process parameters.

Nomenclature	Value
Constant in equation (12), A (Pa)	1.78×10^{10}
Constant in equation (16), A_v	2.52
Vaporization constant in equation (11), B_0	0.55
Speed of light, c (m s^{-1})	3×10^{8}
Specific heat of solid phase, c_s (J kg^{-1} K^{-1})	700
Specific heat of liquid phase, c_l (J kg^{-1} K^{-1})	780
Specific heat of plasma, c_{pl} (J kg^{-1} K^{-1})	900
Charge of electron, e (C)	1.6022×10^{-19}
Ionization potential for neutral atoms, E_i (J)	1.265×10^{-18}
Sulfur concentration in base metal, f^{α} (ppm)	100
Gravitational acceleration, g (m s^{-2})	9.8
Degeneracy factors for electrons, g_e	30
Degeneracy factors for ions, g_i	30
Degeneracy factors for neutral atoms, g_0	25
Quantum mechanical Gaunt factor, $\overline{g}$	1.5
Convective heat transfer coefficient, h_{conv} (W m^{-2} K^{-1})	80
Planck's constant, $\overline{h}$ (J s)	6.625×10^{-34}
Latent heat of fusion, H(J kg^{-1})	2.47×10^{5}
Thickness of substrate metal, H_b (mm)	3.0
Latent heat of vaporization, H_v (J kg^{-1})	6.34×10^{6}
Boltzmann's constant, k_b (J K^{-1})	1.38×10^{-23}
Thermal conductivity of liquid phase, k_l (W m^{-1} K^{-1})	22
Thermal conductivity of plasma, k_{pl} (W m^{-1} K^{-1})	3.74
Thermal conductivity of solid phase, k_s (W m^{-1} K^{-1})	22
Atomic mass, m_a (g)	9.3×10^{-23}
Electron mass, m_e (g)	9.1×10^{-28}
Mach number at the outer of the Knudsen layer, M_K	1.2
Avogadro's number, N_a (mol^{-1})	6.022×10^{23}
Laser power, P_{laser} (W)	1700
Laser beam radius, r_f (mm)	0.2
Laser beam radius at focus, r_{f0} (mm)	0.2
Laser pulse duration t_p (ms)	15
Gas constant, R (J kg^{-1} mol^{-1})	8.3×10^{3}
Radius of substrate metal, R_b (mm)	20.0
Liquidus temperature, T_l (K)	1727
Reference temperature, T_0 (K)	2500
Solidus temperature, T_s (K)	1670
Ambient temperature, T_∞(K)	300
Average ionic charge in the plasma, Z	1
Thermal expansion coefficient, β_T (K^{-1})	4.95×10^{-5}
Surface radiation emissivity, ε	0.4
Dielectric constant, ε_0	14.2
Constant in equation (18), ε_f	0.2
Specific heat ratio, γ_r	1.6
Angular frequency of laser radiation, ω (rad s^{-1})	1.78×10^{14}
Dynamic viscosity, μ_l (kg m^{-1} s^{-1})	0.006
Stefan–Boltzmann constant, σ (W m^{-2} K^{-4})	5.67×10^{-8}
Electrical conductivity, σ_e (Ω^{-1} m^{-1})	7.14×10^{-5}
Density of liquid phase, ρ_l (kg m^{-3})	6900
Density of plasma, ρ_{pl} (kg m^{-3})	0.06
Density of solid phase, ρ_s (kg m^{-3})	7200

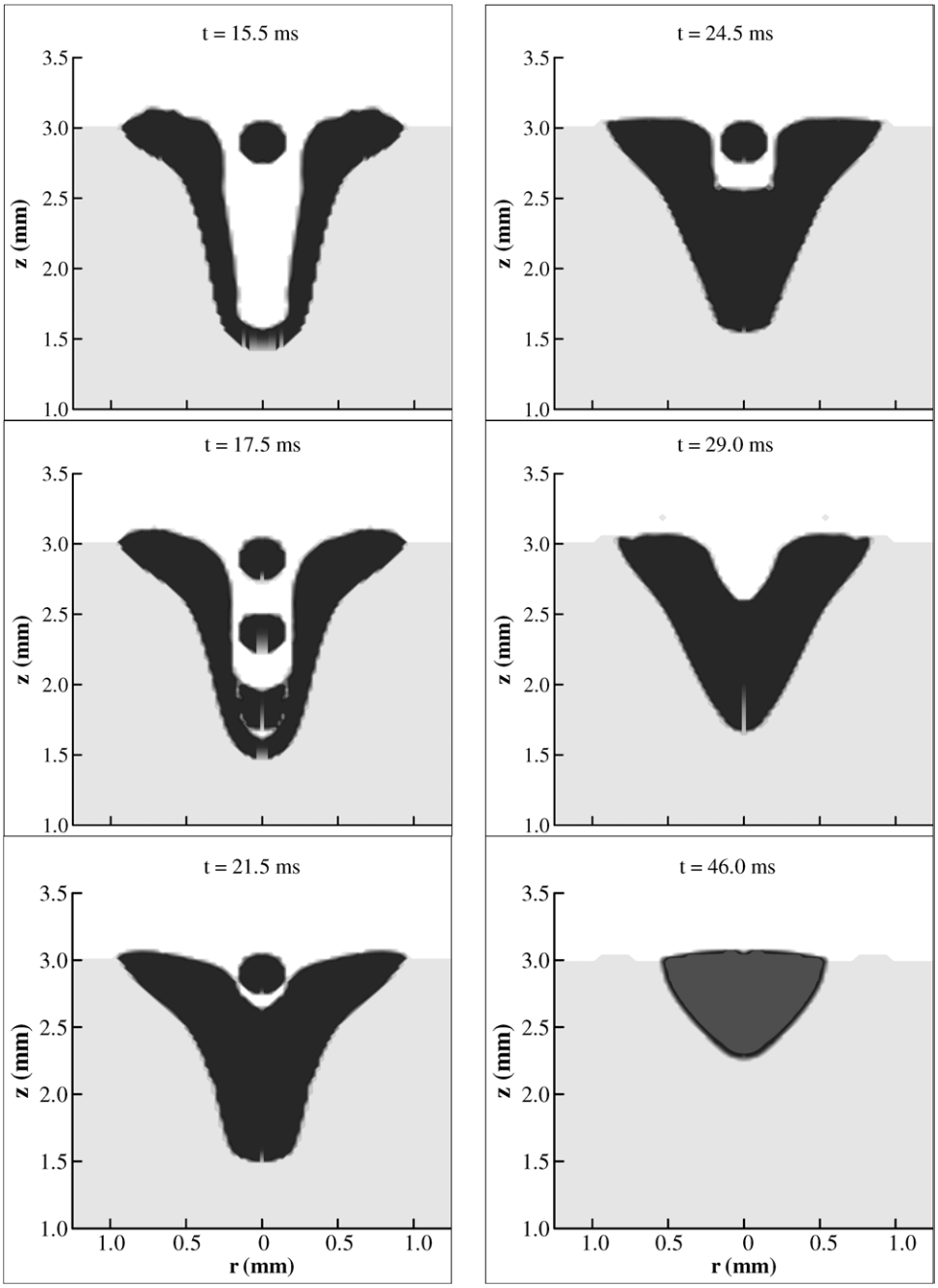

Figure 2. A sequence of metal evolution showing the impingement process of filler metal into the weld pool in hybrid laser–MIG welding.

this sense, the tracing element will not affect the mixing and diffusion processes. In the keyhole plasma model, the metal vapour in the keyhole is assumed to be a compressible, inviscid ideal gas and the generic translation vapour flow along the keyhole is neglected for low power laser keyhole welding [27]. The keyhole plasma is assumed to be an absorbing–emitting medium and the scattering effect is neglected.

4.1. Impingement, mixing and diffusion of filler droplets in weld pool

The laser power used in this study is 1.7 kW with a beam radius of 0.2 mm at the focus. The laser is turned on at $t = 0.0$ ms and lasts for 15 ms. It is assumed that filler droplets are steadily generated via a certain wire feeding method right after the shut-off of the laser. The droplets are made of 304 stainless steel containing 300 ppm sulfur. The diameter of a typical filler droplet is assumed to be 0.35 mm, at the initial impinging speed 0.5 m s^{-1}, initial temperature 2400 K and generation frequency 1000 Hz (i.e. a droplet per 1 ms).

Figure 2 shows the typical impingement and droplet–weld pool interaction processes. The corresponding distributions of temperature, sulfur concentration and fluid flow velocity are given in figures 3, 4 and 5, respectively. Since the interaction between filler droplets and the weld pool is of primary concern in this study, the detailed discussions of keyhole formation and collapse, metal melting and solidification are skipped and

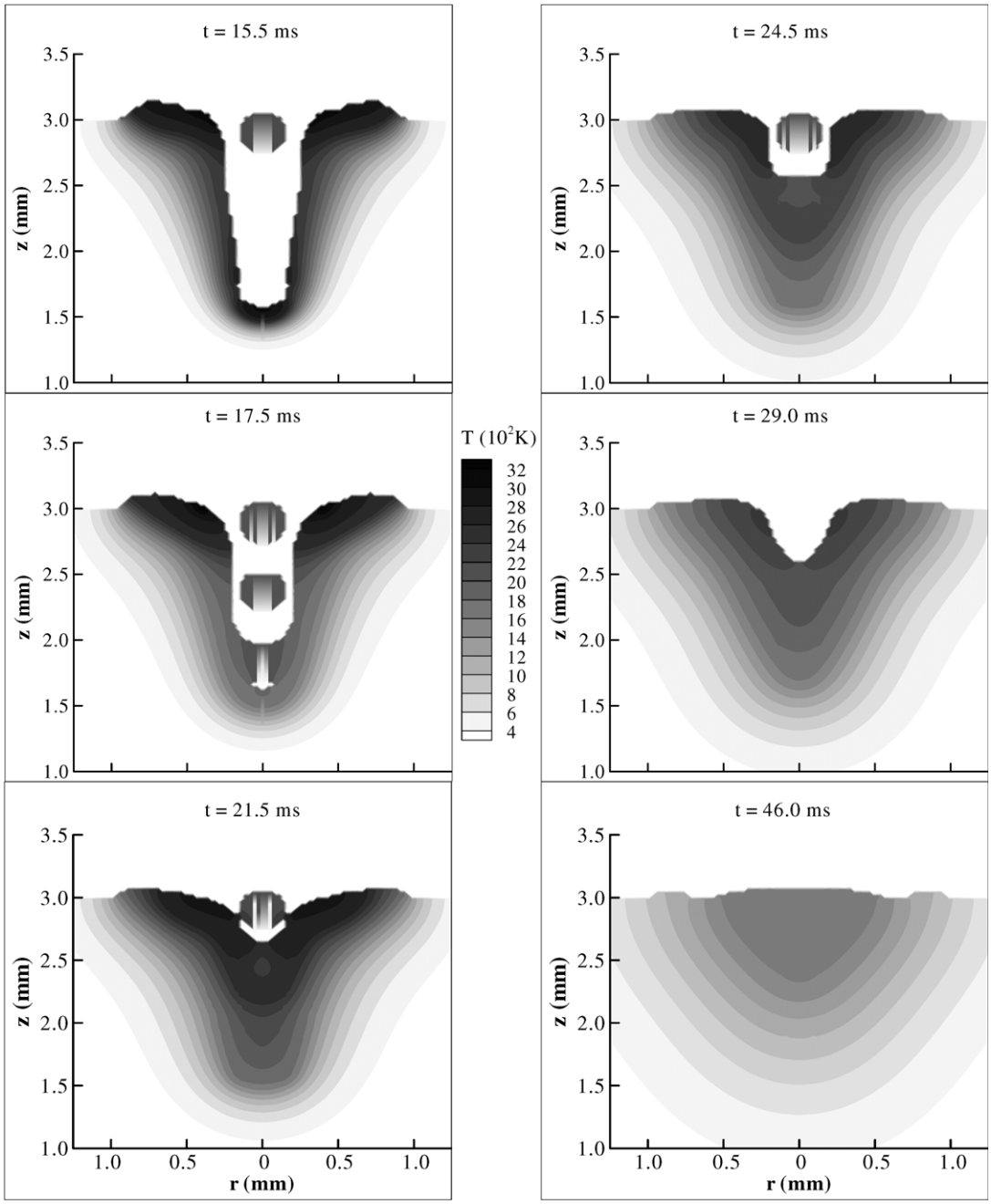

Figure 3. The corresponding temperature distributions as shown in figure 2.

can be found in previous studies [22]. As shown in figure 2, droplets start to fall into the keyhole at $t = 15$ ms. In this study, whenever the droplet is in touch with the weld pool, it will merge into the weld pool and become part of the weld pool. Hence, when the first droplet impinges into the keyhole at around $t = 17.5$ ms, the downward momentum carried by the droplet forces the melt to flow downward and inward along the keyhole wall, which can be found by tracing the sulfur concentration distributions shown in figure 4. When the droplet reaches the bottom of the keyhole, since the melt is incompressible, the downward momentum squeezes some liquid metal against the keyhole bottom and forces it to bounce back to flow upward and outward. Meanwhile, during the keyhole collapse process, the liquid metal along the keyhole wall has a tendency to flow downwards along the keyhole wall under the actions of hydrostatic force and surface tension. When the upward flow meets the downward flow, they exchange momentum, which makes it difficult for the droplet on the top to further flow downward. So, as shown in figure 4 at $t = 21.5$ ms, when the subsequent filler droplets impinge into the keyhole, it is hard for them to reach the bottom of the keyhole. As shown, for the first several droplets, the filler metal mainly diffuses along the longitudinal direction and only the first droplet can spread out along the solid–liquid interface.

As more droplets impinge into the weld pool, as shown in figure 5, in the middle of the keyhole, a counter-clockwise vortex is created by the strong interaction between the droplets and weld pool. The formation of the vortex helps the filler

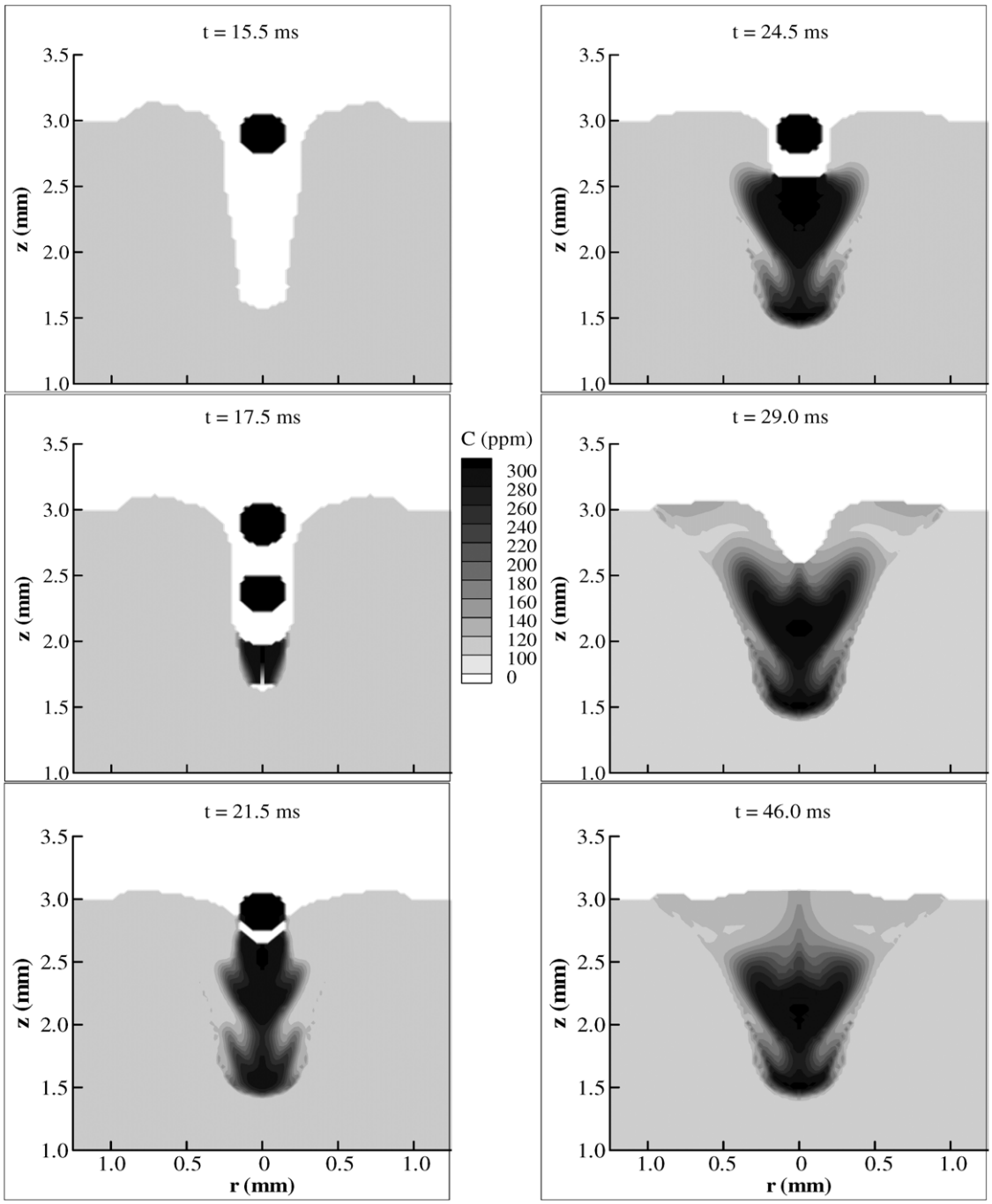

Figure 4. The corresponding sulfur concentration distributions as shown in figure 2.

metal diffuse outwards in a latitudinal direction, as shown in figure 4. As mentioned before, the liquid metal on the shoulder of the keyhole has a tendency to fill back along the keyhole wall during the keyhole collapse process. During the droplet impinging process, the direction of the liquid metal flow on the outer layer along the keyhole wall remains downward. When the droplet hits the keyhole bottom, the downward flow in the centre is bounced back. The kinetic energy of the melt flow is gradually transferred into the potential and kinetic energy of the outward flow. So the original downward momentum of the flow becomes smaller and smaller and finally the flow changes its direction. As shown in figure 5 at $t = 21.5$ ms, the melt flow changes its direction from downward to outward at the bottom of the vortex and then continues to flow upwards. Since the momentum of this upward flow is balanced by momentum of the back-filling flow from the shoulder of the keyhole, the velocity of the upward flow becomes smaller and smaller. Finally, in the upper part of the keyhole, the flow changes its direction again to flow inwards and downwards along the solid–liquid interface of the keyhole wall. Thus, a vortex is created. As droplets continue to drip into the keyhole, more and more momentum is added into the centre of the keyhole, the size of the vortex is enlarged and the strength of the vortex is enhanced. This helps the filler metal diffuse in the latitudinal

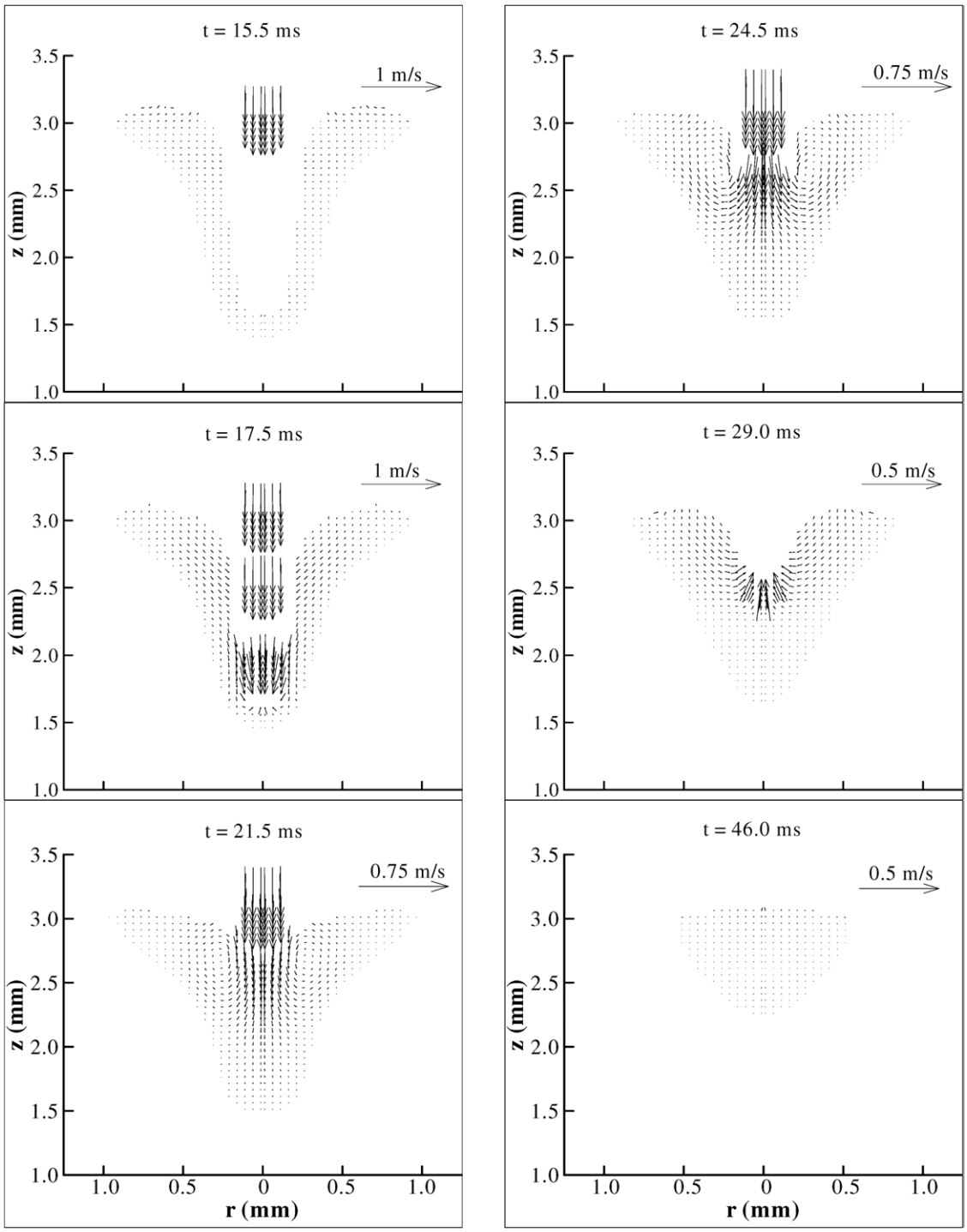

Figure 5. The corresponding velocity distributions as shown in figure 2.

direction. As shown in figure 4, at $t = 24.5$ ms, the diffusion zone of the filler metal is much larger compared with that at $t = 21.5$ ms. Since the latitudinal diffusion of the filler metal has a close relationship with the vortex formation, the evolution of the vortex can be deduced by tracing the change of the sulfur concentration in the fusion zone.

At $t = 25.0$ ms, no droplet is added into the keyhole. The fluid at the centre of the keyhole is bounced back under the action of hydrostatic and surface tension force. As shown at $t = 29.0$ ms in figure 2, the liquid in the keyhole starts to flow inwards and downwards and the size of the keyhole becomes smaller and smaller. Finally, the keyhole will be completely filled back [22]. During this process, the vortex becomes smaller and weaker. So the diffusion of filler metal is not much improved in the latitudinal direction and this can be found by comparing those figures at $t = 29.0$ ms and at $t = 46.0$ ms in figure 4. Moreover, according to the sulfur concentration distribution at $t = 46.0$ ms, it can be deduced that, most of the back-filling metal comes from the upper shoulder of the keyhole because only a small amount of the filler metal is

found near the centre of the keyhole, which is brought here by the bouncing flow.

As shown in figure 4, in hybrid laser welding, filler droplets also bring additional heat into the weld pool, which helps delay the solidification process. Since the diffusion of filler metal in the fusion zone is greatly limited by the solidification, the delayed solidification gives more time for the filler metal to diffuse into the base metal. When the droplet impingement stops, the heat input through droplets also ceases. Due to the fast heat loss to the base metal by conduction and to the surroundings by radiation and convection, the size of the molten pool becomes smaller and smaller as a result of solidification. At $t = 46.0$ ms, when the solidification proceeds, there is only small amount of melt flow left in the weld pool and the temperature distribution is more uniform than before, as shown in figures 3 and 5. The composition in the weld does not change much prior to complete solidification.

4.2. Effect of droplet size on mixing and diffusion

As discussed before, the chemical composition in the melting zone has a close relationship with the crack sensitivity. Hence, adding filler metal with high content of anti-crack elements in welding will be a good way to improve welds' crack resistance. However, good diffusion of filler metal into the base metal is very challenging in hybrid laser welding. In laser welding, the solidification proceeds very fast after the shut-off of the laser due to the high temperature gradient and small weld pool. So the time for diffusion is very short compared to the conventional arc welding process. Uniform distribution of filler metal in the fusion zone is very difficult to achieve if the welding parameters are not properly controlled. So it is important to investigate the factors that affect the diffusion of the filler metal in the fusion zone.

From the above analysis of the mixing and diffusion processes in hybrid laser welding, it is believed that the diffusion of the filler metal into the base metal depends mainly on the following factors: droplet size, droplet generation frequency, initial impinging velocity of droplet, duration of impingement and the rate of solidification. In the following discussion, sulfur concentration is used to trace the diffusion of filler metal in the fusion zone. To determine the influence of a particular process parameter on the diffusion process, the other welding conditions are fixed while the value of that particular parameter is changed. If not specifically mentioned, the welding condition is defined as follows: the diameter of the droplet is 0.35 mm, the initial impinging velocity is 0.5 m s^{-1}, the generation frequency is 1000 Hz and the duration of droplet feeding is 10 ms which starts at $t = 15$ ms.

Figure 6 shows the effect of droplet size on the diffusion of the filler metal into the fusion zone. In hybrid laser welding, the size of the filler droplet can be affected by the diameter of the filler wire, welding current, etc. In this study, three simulations are carried out with droplet sizes of 0.3 mm, 0.35 mm and 0.4 mm, respectively. As shown, with the increase in the droplet diameter, the latitudinal diffusion of filler metal is enlarged. From the previous analysis of the mixing process, the latitudinal diffusion of the filler metal is found to be closely related to the characteristics of the vortex created by the droplet–weld pool interaction. The strength and the size of the vortex depend on the downward momentum carried by the droplets, which is the product of the mass and velocity of the droplet. As the droplet size increases, the downward momentum increases. It creates a stronger and bigger vortex in the weld pool. Thus, diffusion of the filler metal in the fusion zone is improved in the latitudinal direction, especially in the middle depth of the keyhole where the vortex is located. This can be found by comparing those figures for $d = 0.30$ mm and $d = 0.35$ mm in figure 6. Meanwhile, stronger downward momentum from a larger droplet also leads to a stronger bouncing flow near the centre of the keyhole after the termination of droplet feeding. This helps the filler metal to diffuse into the upper part in the final weld, as shown in figure 6 for $d = 0.40$ mm. Moreover, a larger size droplet brings more filler metal into the keyhole, and more heat input, which delays the solidification process in the fusion zone. This gives more time for the filler metal to diffuse in the weld pool. Meanwhile, more filler metal increases the fusion ratio, the ratio of the mass of filler metal to the mass of melted base metal, thus it enhances the filler diffusion in the final weld. However, large-size droplets also bring some negative effects on the diffusion of the filler metal near the centre of the fusion zone. When the droplet feeding stops, the fluid in the centre of the keyhole still carries strong downward momentum and continues to flow downwards. This leads to a deep hole in the centre. During the back-filling process, liquid metal from the upper part of the keyhole flows into the bottom of this hole. Since the concentration of the filler metal in the upper part of the keyhole is very low, a low diffusion zone of filler metal is left in the centre of the final weld, as shown in figure 6 for $d = 0.40$ mm.

4.3. Effect of droplet generation frequency on mixing and diffusion

Figure 7 shows the effect of droplet generation frequency on the diffusion of the filler metal in the fusion zone. In hybrid laser welding, the droplet generation frequency is affected by many factors, such as wire feed speed, welding currents, etc. In this simulation, the droplet generation frequency is at 500 Hz, 667 Hz and 1000 Hz, which corresponds to the generation of one droplet every 2 ms, 1.5 ms and 1 ms, respectively. By comparing those figures shown in figure 7, it is found that an increase in generation frequency can improve the diffusion of the filler metal into welds. This can be interpreted through the analysis of the interaction between filler metal and the weld pool. As mentioned before, the latitudinal diffusion of the filler metal is initiated and mainly controlled by the vortex flow created by the impingement of filler droplets. With the increase in droplet generation frequency, more droplets impinge into the weld pool per unit time. This results in higher downward momentum in the weld pool per unit time. So, the intensity and the size of the vortex are both enhanced, which helps the

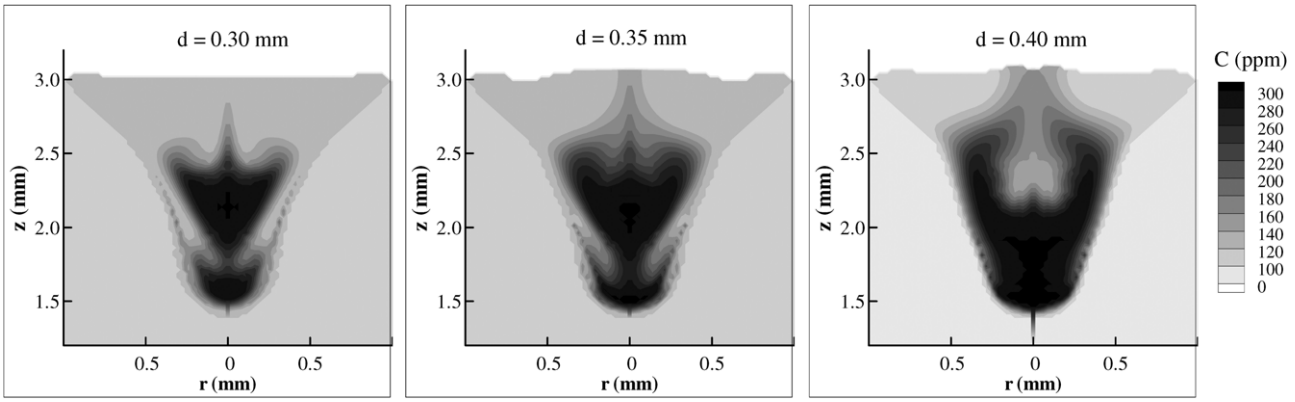

Figure 6. Effect of droplet size on the sulfur distribution in the weld.

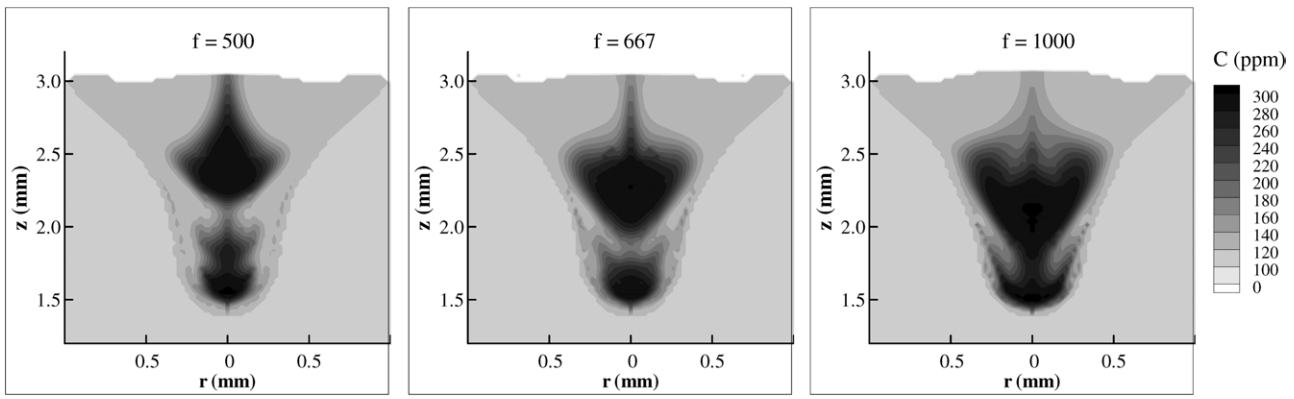

Figure 7. Effect of droplet generation frequency on the sulfur distribution in the weld.

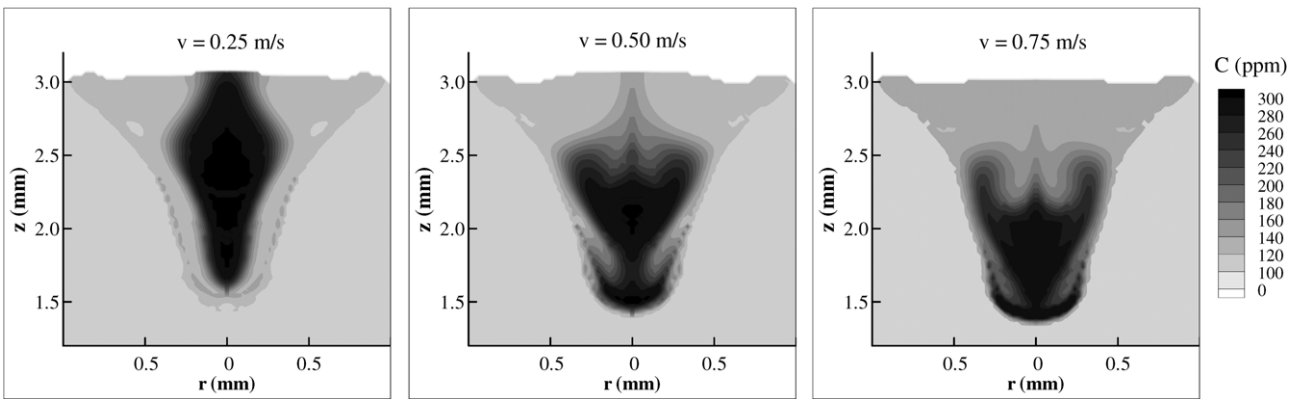

Figure 8. Effect of droplet impinging velocity on the sulfur distribution in the weld.

filler metal to diffuse in the latitudinal direction. Meanwhile, the total amount of filler metal added in the weld pool also increases with higher frequency and this also helps to increase the overall diffusion time and concentration of filler metal in the final weld. Moreover, the longitudinal distribution of the filler metal is also improved with higher generation frequency. As shown in figure 7, for the case of $f = 500$ Hz, there exists a low filler metal concentration zone in the lower part of the keyhole due to a weak vortex and a long time interval between every two impinging droplets. When the generation frequency increases to 1000 Hz, the size of this low filler metal concentration zone is greatly reduced.

4.4. Effect of impinging velocity of filler droplet on mixing and diffusion

In this study, the initial impinging velocity of the droplet is taken as the velocity at the moment when the droplet reaches the top of the keyhole. In hybrid laser welding, the droplet is accelerated under the gravity and arc pressure after it is detached from the filler wire. So the initial impinging velocity of the droplet depends on the distance between the tip of the filler wire and the top surface of the welding coupon, the size of the droplet and the arc pressure. In order to analyse the effect of the initial impinging velocity of the droplet on the diffusion process, three simulations are carried out with

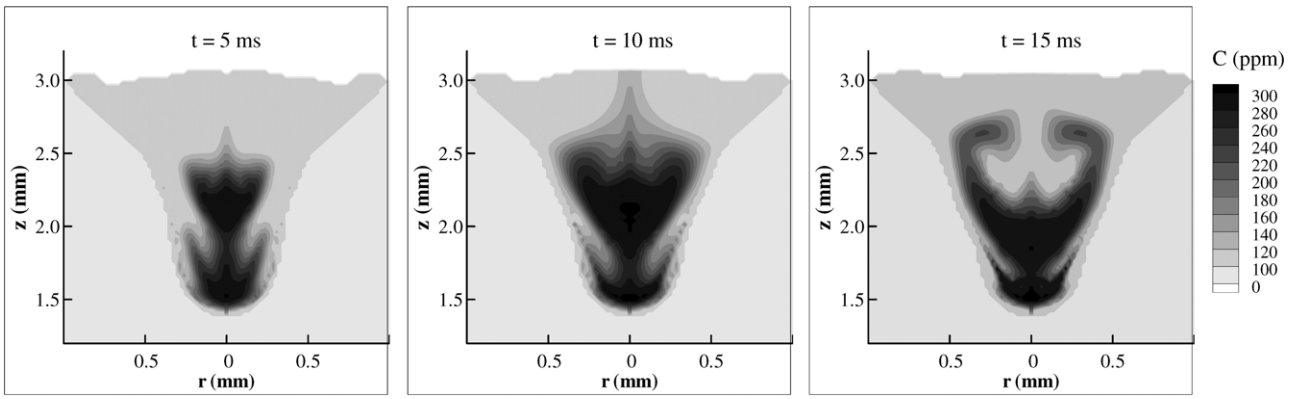

Figure 9. Effect of droplet impinging duration on the sulfur distribution in the weld.

an initial velocity of $0.25\,\mathrm{m\,s^{-1}}$, $0.5\,\mathrm{m\,s^{-1}}$ and $0.75\,\mathrm{m\,s^{-1}}$, respectively. As shown in figure 8, with the increase in droplet impinging velocity, the latitudinal diffusion of the filler metal is improved. This can be explained by analysing the interaction between the droplet and the weld pool. As shown before, the latitudinal diffusion process is closely related to the size and strength of the vortex created by the downward momentum of the liquid metal. The increase in droplet velocity brings stronger downward momentum into the weld pool, thus a stronger vortex, which helps the filler to diffuse outwards along with the vortex flow. Compared with that for $v = 0.25\,\mathrm{m\,s^{-1}}$, the latitudinal diffusion of filler metal in the welds is improved at $v = 0.5\,\mathrm{m\,s^{-1}}$, especially in the vortex-affected zone. However, stronger downward momentum also pushes down the fluid surface level near the centre of keyhole, which prevents the filler metal from flowing and diffusing upwards. In the case of $v = 0.25\,\mathrm{m\,s^{-1}}$, the downward momentum carried by the filler droplets is relatively small, and the fluid surface near the centre of the keyhole is only slightly pushed down by the downward momentum. The filler metal almost stays in the position where the filler droplets impinge into the weld pool and it is difficult for the base metal liquid to reach the centre of the keyhole. Hence, the latitudinal diffusion of the filler metal is very limited. In the case of $v = 0.75\,\mathrm{m\,s^{-1}}$, the larger downward momentum pushes down the fluid in the centre of the keyhole to create a deeper hole. When the droplet feeding stops, it takes some time for the fluids on the bottom of the hole to bounce back. Similar to the keyhole collapse process, the keyhole is filled back almost completely by the base metal and the diffusion of the filler metal in the upper part of weld is poor. However, the diffusion of the filler metal near the bottom of the keyhole is improved with the increase in droplet velocity. As discussed before, the diffusion near the bottom depends mainly on the impingement of the first droplet. For a lower initial droplet velocity of $v = 0.25\,\mathrm{m\,s^{-1}}$, the downward momentum is not large enough to force the filler metal to spread out along the bottom of the keyhole. Also, with the increase in the droplet impinging velocity, the stronger downward momentum helps the filler metal spread out along the solid–liquid interface near the bottom of the keyhole.

4.5. Effect of impinging duration of filler droplet on mixing and diffusion

In hybrid laser welding, the termination of droplet generation can be controlled by the removal of the filler wire. The effect of this parameter on diffusion is investigated through simulations with different durations. As shown in figure 9, three cases are carried out. Their durations are 5 ms, 10 ms and 15 ms, respectively. For a short duration, the vortex induced by the downward momentum of the droplet is not completely developed because of lower downward momentum, which leads to poor latitudinal distribution of the filler metal. Meanwhile, during the back-filling process, the bounced flow is not strong enough to push the filler metal upwards to the upper part of the keyhole. Most of the filler metal is located in the lower part of the keyhole and the keyhole is filled with the base metal liquid where almost no filler metal exists. So the longitudinal filler diffusion is poor with a short duration of droplet generation. With the increase in duration length, more filler metal drips into the keyhole. The vortex is enhanced by the increase in the downward momentum which improves the latitudinal diffusion. Meanwhile, with the increase in duration length, more filler droplets are distributed along the whole depth of the keyhole and this also leads to a better longitudinal distribution of the filler metal, as shown in figure 9. However, with the increase in the duration length, more downward momentum is accumulated as droplets impinge into the weld pool, which can lead to a deeper hole. During the back-filling process, the filler fluid mainly stays in the bottom, and cannot bounce back in time before the base metal fluid from the upper shoulder arrives at the bottom of this hole, which causes a low diffusion zone of filler metal in the centre of the final weld, as shown in figure 9.

4.6. Combined effect of droplet size and droplet frequency on mixing and diffusion

Figure 10 shows the combined effect of droplet size and generation frequency on the diffusion of the filler metal in the fusion zone with equal mass. In the previous cases, the influences of droplet size and generation frequency on the diffusion of the filler metal in the fusion zone were studied separately. However, in reality, the filler droplet size

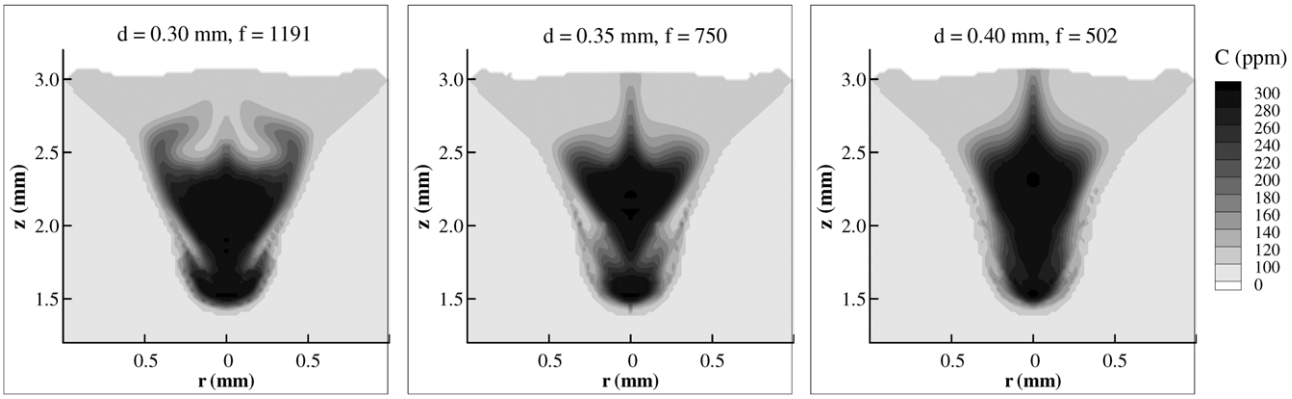

Figure 10. Combined effect of droplet size and droplet frequency on the sulfur distribution in the weld.

and generation frequency are related. In order to analyse the effect of droplet size and generation frequency without the interference of droplet mass, simulations are carried out with three combinations of droplet size and generation frequency: droplet diameter of 0.3 mm at a generation frequency of 1191 Hz; droplet diameter of 0.35 mm at a generation frequency of 750 Hz; droplet diameter of 0.4 mm at a generation frequency of 502 Hz. As shown in the figure, the latitudinal diffusion of filler metal is improved while the longitudinal diffusion of filler metal is worsened with the increase in generation frequency and the decrease in droplet size. This can be explained through the analysis of the interaction between the droplet and the weld pool. As discussed, the latitudinal diffusion process depends on the size and strength of the vortex created by the downward momentum of the melt. With smaller droplet size and higher generation frequency, the downward momentum is added into the weld pool gradually. In this case, the fluid surface near the centre of the keyhole does not fluctuate much and most of the downward momentum is used to develop the vortex in the fusion zone. However, with larger droplet size and lower generation frequency, the fluid surface near the centre is pushed down more by the larger filler droplet with stronger downward momentum. Since the interval of the droplets' impingement is longer, the fluid surface is able to bounce back. This makes the fluid surface fluctuate upwards and downwards, which absorbs the downward momentum from the impinging droplets. Then, it is difficult for the vortex to develop in the fusion zone compared with that for smaller droplet size and higher generation frequency. However, the fluctuation of the fluid surface near the centre of the weld pool helps the filler metal diffuse in the longitudinal direction, which results in better longitudinal diffusion of the filler metal compared with that for smaller droplet size and higher generation frequency.

5. Conclusions

Mathematical models have been developed to investigate the mixing and diffusion processes in hybrid laser–MIG welding by tracing the distribution of sulfur concentration in the fusion zone. The effects of the key parameters, such as droplet size (wire diameter), droplet generation frequency (wire feed speed) and droplet impinging speed, on mixing and diffusion are systematically investigated.

As shown in the study, the mixing and diffusion of the filler droplets into the base metal is greatly affected by the dynamics of the weld pool fluid flow. The competition between the rate of mixing and the rate of solidification determines the compositional homogeneity of the weld pool. Increasing the filler droplet size can create a stronger and larger vortex in the weld pool. A stronger and larger vortex can thus improve the latitudinal diffusion of the filler droplet in the fusion zone. However, larger droplets are also easy to create a low diffusion zone of filler metal at the centre of the final weld due to the strong downward momentum carried into the weld pool by the droplets. Droplet frequency and impinging velocity also affect the mixing and diffusion processes. A small-size filler droplet combined with high generation frequency can increase the latitudinal diffusion, while the large-size droplet combined with the low generation frequency helps to get more uniform longitudinal diffusion. Increasing the filler droplet impinging velocity can improve the latitudinal diffusion of filler metal. However, high impinging velocity can cause the low filler metal diffusion zone in the upper part of the welds. In summary, this study provides a good foundation for the optimization of the hybrid laser–MIG welding process (controlling the filler wire feeding) to achieve quality welds with the desired properties.

Acknowledgment

It is gratefully acknowledged that this research is partially supported by the General Motors Corporation.

References

[1] Duley W W 1999 *Laser Welding* (New York: Wiley)
[2] Schinzel C, Hohenberger B, Dausinger F and Hügel H 1998 *Proc. ICALEO (Orlando, FL)* Section F p 56
[3] Connor L P 1987 *Welding Handbook* 8th edn (New York: American Welding Society)
[4] Hatch J E 1984 *Aluminum: Properties and Physical Metallurgy* (Russell, OH: American Society for Metals)
[5] Cieslak M J and Fuerschbach P W 1988 *Metall. Trans.* B **19** 319
[6] Dudas J H and Collins F R 1966 *Weld. J.* **45** 241s

[7] Ono M, Shinbo Y, Yoshitake A and Ohmura M 2002 *NKK Techn. Rev.* **86** 8
[8] Weisheit A, Galun R and Mordike B L 1998 *Weld. J.* **77** 149s
[9] Kutsuna M and Chen L 2002 *Proc. SPIE* **4831** 341
[10] Ishide T, Tsubota S and Watanabe M 2002 *Proc. SPIE* **4831** 347
[11] Staufer H, Rührnößl M and Miessbacher G 2003 *Ind. Laser Solut.* **7**
[12] Engström H, Nilsson K, Flinkfeldt J, Nilsson T, Skirfors A and Gustavsson B 2001 *Proc. ICALEO (Jacksonville, FL)* 2001 p 125
[13] Missouri S and Sili A 2000 *Weld. J.* **79** 317
[14] Hwang J R, Doong J L and Chen C C 1996 *Mater. Trans. J.* **37** 1443
[15] Schubert E, Klassen M, Skupin j and Sepold G 1998 *Int. Conf. on Welding and Melting by Electron Laser Beams (Toulon, France)* p 195
[16] Moore P L, Howse D S and Wallach E R 2004 *Sci. Technol. Weld. Joining* **9** 314
[17] Hu B and Richardson I M 2007 *Mater. Sci. Eng.* A **459** 94
[18] Fellman A, Kujanpaa V 2006 *J. Laser Appl.* **18** 12
[19] Campana G, Fortunato A, Ascari A, Tani G and Tomesani L 2007 *J. Mater. Process. Technol.* **191** 111
[20] Kim C, Choi W, Kim J, Rhee S 2008 *Mater. Trans.* **49** 179
[21] Sun S and Moisio T 1993 *Mater. Sci. Technol.* **9** 603
[22] Zhou J and Tsai H L 2008 *Int. J. Heat Mass Transfer* **57** 4353
[23] Naito Y, Katayama S and Matsunawa A 2002 *Proc. SPIE* **4831** 357
[24] Zhao H and Debroy T 2001 *Metall. Mater. Trans.* B **32** 163
[25] Kothe D B, Mjolsness R C and Torrey M D 1991 *Ripple: A Computer Program for Incompressible Flows with Free Surfaces* LA-12007-MS (Los Alamos National Laboratory)
[26] Chiang K C and Tsai H L 1992 *Int. J. Heat Mass Transfer* **35** 1763
[27] Miyamoto I, Ohmura E and Maede T 1997 *Proc. ICALEO (San Diego, CA)* Section G p 210
[28] Dowden J, Postacioglu N, Davis M and Kapadia P 1987 *J. Phys. D: Appl. Phys.* **20** 36
[29] Ishide T, Tsubota S, Nayama M, Shimokusu Y, Nagashima T, Okimura K 1999 *SPIE High-Power Lasers Manuf., Proc. SPIE* **3888** 543
[30] Wang Y and Tsai H L 2001 *Int. J. Heat Mass Transfer* **44** 2067
[31] Sahoo P, DeBroy T and Mcnallan M J 1988 *Metall. Trans.* B **19** 483
[32] Choo R T C, Szekely J and David S A 1992 *Metall. Trans.* B **23** 371
[33] Knight C J 1979 *AIAA J.* **17** 519
[34] Semak V and Matsunawa A 1997 *J. Phys. D: Appl. Phys.* **30** 2541–52
[35] Zacharia T, David S A and Vitek J M 1991 *Metall. Trans.* B **22** 233
[36] Raizer Y P 1977 *Laser-induced Discharge Phenomena* (New York: Consultants Bureau)
[37] Spitzer L 1967 *Physics of Fully Ionized Gases* (New York: Interscience)
[38] Kogelnik H and Li T 1966 *Appl. Opt.* **5** 1550
[39] Siegel R and Howell J R 1992 *Thermal Radiation Heat Transfer* 3rd edn (New York: Hemisphere) Chapter 13
[40] Ho R, Grigoropoulos C P and Humphrey J A C 1996 *J. Appl. Phys.* **79** 7205
[41] Zhu F L, Tsai H L, Marin S P and Wang P C 2004 *Prog. Comput. Fluid Dyn.* **4** 99